Higher-Order Spatial Discretization for Turbulent Aerodynamic Computations

S. De Rango* and D. W. Zingg†
University of Toronto, Toronto, Ontario M3H 5T6, Canada

A higher-order spatial discretization is presented for the solution of the thin-layer Navier–Stokes equations with application to two-dimensional turbulent aerodynamic flows. The terms raised to a level of accuracy consistent with third-order global accuracy include the inviscid and viscous fluxes, the metrics of the generalized curvilinear coordinate transformation, the diffusive fluxes in the turbulence model, the numerical boundary schemes, and the numerical integration technique used to calculate forces and moments. Given the presence of grid and flow singularities, third-order convergence behavior is not expected. The motivation is to reduce the numerical error on a given grid or to reduce the grid density required to achieve specified error levels. Results for several grid convergence studies show that this higher-order approach produces a substantial reduction in numerical error in the computation of single- and multielement aerodynamic flows, both subsonic and transonic. Comparisons with a well-established second-order algorithm demonstrate that significant savings in computing expense, typically factors of three to four, can be achieved using the higher-order discretization.

Introduction

ONE way to improve the efficiency of a flow solver for the compressible Navier–Stokes equations is to raise the accuracy of the spatial discretization, thereby reducing the number of grid nodes required to achieve a solution of a given numerical accuracy. The potential of higher-order methods (which we define to be methods of order three or greater) to reduce the cost of numerical solutions of hyperbolic partial differential equations has been recognized for a long time.[1,2] In applications requiring high accuracy, such as direct simulations of turbulent flows,[3,4] aeroacoustics,[5,6] electromagnetics,[7,8] and complex unsteady flows,[9,10] the use of higher-order methods is an active area of research. The application of higher-order methods to steady aerodynamic flows has been more limited, despite showing considerable promise.[11−17]

One issue delaying the impact of higher-order methods in computing aerodynamic flows is the need for numerical dissipation in the discretization of the inviscid flux terms. Initially, the most popular approach was the scalar dissipation scheme of Jameson et al.[18] It has since been recognized that this scheme can be a major source of error in the computation of boundary layers.[19,20] The introduction of more sophisticated schemes for adding numerical dissipation, such as flux-difference splitting[21] and matrix dissipation,[22] has greatly reduced the resulting errors, thus paving the way for the use of higher-order methods. Another impediment to the use of higher-order methods is the need for stable numerical boundary schemes of suitable accuracy. The use of low-order numerical boundary schemes can greatly undermine the benefits of a higher-order scheme in the interior of the computational domain. Similarly, there is little point in using a higher-order discretization together with a low-order integration technique for calculating forces and moments, especially considering that the integration is a postprocessing step that needs to be performed only once.

To demonstrate the benefits of a higher-order spatial discretization, a technique for determining numerical error is required. The development of such techniques has become an area of considerable interest, as discussed by Roache.[23] In two dimensions it is practical to compare the solution computed on a given grid with another computed on a much finer grid. Assuming that the numerical error on

the latter is negligible relative to that on the former, the difference between the two solutions provides an estimate of the numerical error on the coarser grid. Such grid convergence studies have been used extensively by Zingg.[24]

Zingg et al.[25] performed a detailed study of several spatial discretizations, including a higher-order scheme, in the context of turbulent aerodynamic flows over single-element airfoils. Turbulence was modeled using the algebraic Baldwin–Lomax model. They concluded that significant error reduction can be achieved using a consistent higher-order discretization. Their results show that with modern numerical dissipation schemes, including matrix dissipation,[22] upwinding,[21] and the convective upstream split pressure scheme,[26,27] dissipation is not the leading source of error. Furthermore, they demonstrate that raising the inviscid flux approximation to higher order is ineffective unless the approximation used in calculating the grid metrics is also raised to higher order.

In this paper we extend the higher-order discretization presented by Zingg et al.[25] to incorporate the one-equation turbulence model of Spalart and Allmaras[28] and multiblock grids. These extensions permit application to complex turbulent flows over high-lift multielement airfoil configurations. Such flowfields include confluent boundary layers and wakes as well as regions of separated flow in coves. Nelson et al.[29] showed that the flowfield about a three-element configuration computed using a second-order discretization can contain significant numerical error even with a high-quality grid containing over 100,000 nodes. Hence there is considerable motivation to apply higher-order discretizations to multielement airfoil flows in order to reduce the grid density requirements.

Our objective is to examine the tradeoffs associated with the use of the higher-order discretization and to investigate the impact on the efficiency of the flow solver. We present the details of the discretization followed by a series of systematic grid convergence studies for practical aerodynamic flows, both subsonic and transonic, including a computation for a three-element high-lift configuration. The grid convergence studies provide reliable quantitative estimates of the numerical errors on various grids. Based on these error estimates, the overall efficiency of the higher-order discretization is compared with that of a popular second-order discretization.

Numerical Method and Governing Equations

The basic algorithm parallels that in ARC2D,[30] which is closely related to the widely used code OVERFLOW.[31] We use the diagonal form[32] of the Beam–Warming approximate factorization algorithm[33] with local time stepping to solve the thin-layer Navier–Stokes equations. The Spalart–Allmaras turbulence model requires the solution of a partial differential equation governing the transport of an eddy-viscosity-like quantity. This equation is decoupled

*Graduate Student, Institute for Aerospace Studies, 4925 Dufferin Street; stan@oddjob.utias.utoronto.ca.

†Professor, Institute for Aerospace Studies, 4925 Dufferin Street; dwz@oddjob.utias.utoronto.ca. Senior Member AIAA.

from the mean-flow equations and also solved using the approximate factorization algorithm. Single-element airfoils are handled using single-block grids with a C topology. Multiblock H grids are used for multielement airfoils. The blocks are patched with point and slope continuity. The treatment of block interfaces is discussed later, whereas further details and second-order solutions of multielement flowfields are given in Nelson at al.[34] and Godin et al.[35]

The spatial derivatives are approximated using finite-difference approximations in generalized curvilinear coordinates. In two-dimensional generalized coordinates the thin-layer Navier–Stokes equations are given by[30]

$$\frac{\partial \hat{Q}}{\partial t} + \frac{\partial \hat{E}}{\partial \xi} + \frac{\partial \hat{F}}{\partial \eta} = \frac{\partial \hat{S}}{\partial \eta} \qquad (1)$$

where $\hat{Q} = J^{-1}Q = J^{-1}[\rho, \rho u, \rho v, e]^T$ is the vector of conservative dependent variables, $\hat{E}$ and $\hat{F}$ are the inviscid flux vectors, $\hat{S}$ is the viscous flux vector, ξ and η are the streamwise and normal generalized coordinates, respectively, and J is the Jacobian of the coordinate transformation.

Higher-Order Algorithm

The inviscid fluxes are approximated using a fourth-order centered operator plus a third-order matrix dissipation term, which reduces to first order at shocks. The use of fourth-difference (third-order) dissipation necessitates the use of a five-point stencil and thus the solution of pentadiagonal systems. Increasing the accuracy of the centered difference operator to fourth order does not increase the stencil size, and the overall increase in computing expense per grid node is small. A fourth-order operator is used for the viscous fluxes. Grid metrics are evaluated using the same operators as the convective fluxes without any numerical dissipation. Gustafsson[36] has shown that the numerical boundary schemes can be one order lower than the interior scheme without reducing the global order of accuracy. Hence we can use second-order numerical boundary schemes while preserving third-order global accuracy. Nevertheless, we use third-order boundary schemes whenever they are found to be stable. Overall, the higher-order algorithm costs roughly 6–7% more per iteration than a second-order algorithm using the same numerical dissipation scheme.

Inviscid Fluxes

The following operators are used to approximate first derivatives. Interior (fourth-order):

$$\delta_x q_j = (1/12\Delta x)(-q_{j+2} + 8q_{j+1} - 8q_{j-1} + q_{j-2}) \qquad (2)$$

First interior node (third order):

$$\delta_x q_j = (1/6\Delta x)(-2q_{j-1} - 3q_j + 6q_{j+1} - q_{j+2}) \qquad (3)$$

Boundary (third order):

$$\delta_x q_j = (1/24\Delta x)(-11q_j + 18q_{j+1} - 9q_{j+2} + 2q_{j+3}) \qquad (4)$$

The last equation is required only for the calculation of grid metrics.

In the absence of discontinuities, the matrix dissipation scheme used is third-order accurate. The basic operator is

$$(1/\Delta x)(q_{j-2} - 4q_{j-1} + 6q_j - 4q_{j+1} + q_{j+2}) \qquad (5)$$

At near-boundary nodes the following operator is used for the dissipation:

$$(1/\Delta x)(-q_{j-1} + 3q_j - 3q_{j+1} + q_{j+2}) \qquad (6)$$

Viscous Fluxes

The viscous terms are in the following general form:

$$\partial_x(\alpha_j \, \partial_x \beta_j) \qquad (7)$$

A fourth-order expression is used to calculate the $\partial_x \beta_j$ term at half nodes:

$$(\delta_x \beta)_{j+\frac{1}{2}} = (1/24\Delta x)(\beta_{j-1} - 27\beta_j + 27\beta_{j+1} - \beta_{j+2}) \qquad (8)$$

Near boundaries a third-order expression is used:

$$(\delta_x \beta)_{j+\frac{1}{2}} = (1/24\Delta x)(-23\beta_j + 21\beta_{j+1} + 3\beta_{j+2} - \beta_{j+3}) \qquad (9)$$

The value of $\alpha_{j+\frac{1}{2}}$ in Eq. (7) is determined using the following fourth-order interpolation formula:

$$\alpha_{j+\frac{1}{2}} = \tfrac{1}{16}(-\alpha_{j-1} + 9\alpha_j + 9\alpha_{j+1} - \alpha_{j+2}) \qquad (10)$$

Near boundaries a third-order formula is used:

$$\alpha_{j+\frac{1}{2}} = \tfrac{1}{8}(3\alpha_j + 6\alpha_{j+1} - \alpha_{j+2}) \qquad (11)$$

The complete operator is then

$$\delta_x(\alpha_j \delta_x \beta_j) = (1/24\Delta x)\Big[\alpha_{j-\frac{3}{2}}(\delta_x\beta)_{j-\frac{3}{2}} - 27\alpha_{j-\frac{1}{2}}(\delta_x\beta)_{j-\frac{1}{2}}$$
$$+ 27\alpha_{j+\frac{1}{2}}(\delta_x\beta)_{j+\frac{1}{2}} - \alpha_{j+\frac{3}{2}}(\delta_x\beta)_{j+\frac{3}{2}}\Big] \qquad (12)$$

in the interior and

$$\delta_x(\alpha_j \delta_x \beta_j) = (1/24\Delta x)\Big[-23\alpha_{j-\frac{1}{2}}(\delta_x\beta)_{j-\frac{1}{2}} + 21\alpha_{j+\frac{1}{2}}(\delta_x\beta)_{j+\frac{1}{2}}$$
$$+ 3\alpha_{j+\frac{3}{2}}(\delta_x\beta)_{j+\frac{3}{2}} - \alpha_{j+\frac{5}{2}}(\delta_x\beta)_{j+\frac{5}{2}}\Big] \qquad (13)$$

near boundaries.

Turbulence Model

For the Spalart–Allmaras turbulence model a first-order upwind scheme is used for the convective terms in order to maintain positivity of the eddy viscosity. We have experimented with a third-order upwind-biased treatment of the convective terms and seen no degradation in accuracy associated with the use of the first-order operator. One might consider the use of a flux limiter to ensure positivity while retaining higher-order accuracy in regions where the limiter is inactive. However, the additional cost and possible effect on convergence is not justified, given that the use of a third-order scheme produces no apparent improvement. For single-block grids the diffusive terms are handled in the same manner as the viscous terms described in the preceding subsection. For multiblock grids the diffusive terms are approximated using a second-order scheme, again with no apparent degradation in solution accuracy.

Boundary Conditions

The value of $\hat{Q}$ at a far-field boundary node is calculated as follows[37]:

$$\hat{Q}_{bc} = \tfrac{1}{2}(\hat{Q}_\infty + \hat{Q}_{ext}) - \tfrac{1}{2}\text{sign}(\widehat{A}_\kappa)(\hat{Q}_\infty - \hat{Q}_{ext})$$
$$\text{sign}(\widehat{A}_\kappa) = T_\kappa \,\text{sign}(\Lambda_\kappa) T_\kappa^{-1} \qquad (14)$$

where κ is chosen in the direction normal to the boundary, bc indicates the boundary value, ∞ indicates values obtained from freestream conditions, and ext indicates values extrapolated from the interior nodes of the mesh. The eigenvalues Λ_κ and eigenvectors T_κ of $\widehat{A}_\kappa$ are calculated from the mean state $\hat{Q}_{avg} = \tfrac{1}{2}(\hat{Q}_\infty + \hat{Q}_{ext})$. The following second-order extrapolation operator is used at the far-field boundary:

$$q_j = 3q_{j+1} - 3q_{j+2} + q_{j+3} \qquad (15)$$

A far-field circulation correction is also included.[30]

The pressure at the airfoil surface is determined from a third-order approximation to $\partial p/\partial n = 0$, which gives

$$p_1 = \tfrac{1}{11}(18p_2 - 9p_3 + 2p_4) \qquad (16)$$

For an adiabatic wall $\partial T/\partial n = 0$, and, when coupled with the assumption of zero pressure gradient and the perfect gas law, this
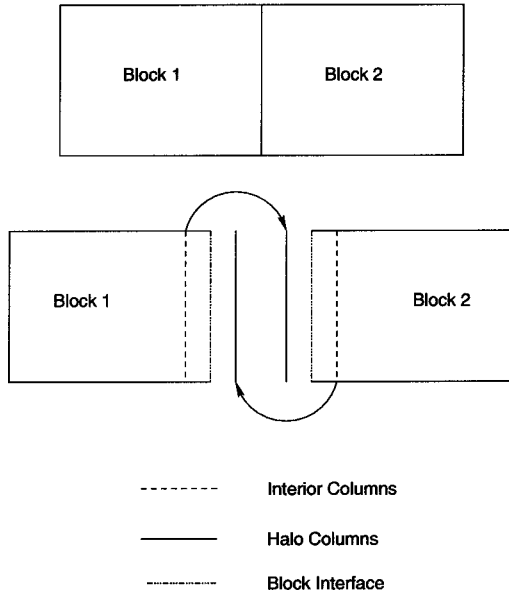
Fig. 1   Two-block grid showing halo data.

implies $\partial \rho / \partial n = 0$. Hence the density at the airfoil surface is determined from an expression analogous to Eq. (16). Although the assumption that $\partial p / \partial n = 0$ is not strictly correct, for aerodynamic flows at high Reynolds numbers the error introduced is very small. We have experimented with higher-order extrapolation of pressure with no significant change in the solution.

On the wake cut (wc) of a single-block C grid, the solution is computed to fourth-order using the data above and below the wake cut as follows:

$$q_{k_{wc}} = \tfrac{1}{6}\left(-q_{k_{wc}+2} + 4q_{k_{wc}+1} + 4q_{k_{wc}-1} - q_{k_{wc}-2}\right) \qquad (17)$$

Treatment of Block Interfaces

For multiblock H grids neighboring block boundaries in the streamwise direction are overlapped at the interfaces. A specified number of columns of points is taken from the neighboring block (known as the halo column). Consider the rectangular two-block grid in Fig. 1. For simplicity, only one halo column will be considered here. The first interior column of block 2 is stored in the halo column of block 1, and the last interior column of block 1 is stored in the halo column of block 2. Blocks 1 and 2 are then updated independently, resulting in two solutions at the block interface. The two interface solutions are subsequently averaged. At steady state the streamwise interface is completely transparent. Block interfaces in the cross-stream direction are treated like wake cuts [Eq. (17)].

Integration

To preserve the accuracy provided by a higher-order solution, it is necessary to use a higher-order integration technique in calculating forces and moments. The following expressions are used to evaluate the normal force C_N and axial force C_A coefficients with respect to the chord line. (For ease of presentation, we consider the pressure contribution only.)

$$C_N = \frac{1}{c}\oint -C_p(\hat{n}\cdot\hat{i})\,\mathrm{d}s \qquad (18)$$

$$C_A = \frac{1}{c}\oint -C_p(\hat{n}\cdot\hat{j})\,\mathrm{d}s \qquad (19)$$

where c is the chord length, s is the arclength along the airfoil surface, x and y are the Cartesian coordinates, and $\hat{i}$ and $\hat{j}$ are unit vectors in the x, y coordinate directions, respectively. The unit normal with respect to the surface $\hat{n}$ is given by

$$\hat{n} = \frac{-(\mathrm{d}y/\mathrm{d}s)\hat{i} + (\mathrm{d}x/\mathrm{d}s)\hat{j}}{\sqrt{(\mathrm{d}x/\mathrm{d}s)^2 + (\mathrm{d}y/\mathrm{d}s)^2}} \qquad (20)$$

We integrate the pressure and shear stress distributions with respect to the arclength around the airfoil. This avoids any possible singularities near the leading or trailing edges.

A cubic spline is used to fit a curve through the nodes making up the airfoil surface. The spline allows for the third-order interpolation of $\mathrm{d}x/\mathrm{d}s$ and $\mathrm{d}y/\mathrm{d}s$ at any point on the airfoil surface. The pressure distribution is also splined. We have examined the resulting interpolant for flows with shocks and seen no oscillations. An adaptive quadrature routine is used to integrate Eqs. (18) and (19). The quadrature routine uses the two-point Gauss–Legendre rule as the basic integration formula with a global error-control strategy. Details regarding the mechanics of the global strategy can be found in Malcolm and Simpson.[38]

Left-Hand Side

The linearization of the right-hand-side operator required for the implicit algorithm is carried out such that a pentadiagonal left-hand-side operator is obtained. Because the fourth-order viscous operator just described leads to a seven-point stencil, the standard second-order operator is used on the left-hand side. Approximate linearizations are used for some of the near-boundary operators as well.

Test Cases and Grids

Grid convergence studies are presented for the following four test cases:

1) NACA 0012 airfoil, $M_\infty = 0.16$, $\alpha = 12$ deg, $Re = 2.88 \times 10^6$, laminar-turbulent transition at 0.01 and 0.95 chords on the upper and lower surfaces, respectively: Boundary-layer separation occurs on the upper surface near the trailing edge. Experimental data can be found in Gregory and O'Reilly.[39]

2) NACA 0012 airfoil, $M_\infty = 0.7$, $\alpha = 3$ deg, $Re = 9.0 \times 10^6$, laminar-turbulent transition at 0.05 chords on both surfaces: This case and case 3 are transonic flows with shock waves of moderate strength.

3) RAE 2822 airfoil, $M_\infty = 0.729$, $\alpha = 2.31$ deg, $Re = 6.5 \times 10^6$, laminar-turbulent transition at 0.03 chords on both surfaces: The measured coordinates for the RAE 2822 airfoil are used, rather than the standard coordinates. Experimental data for case 3 can be found in Cook et al.[40]

4) Case A-2 from Moir,[41] model designation NHLP 2D: The specific case is L1T2, which includes a 12.5%c leading-edge slat and a 33%c single-slotted flap, where c is the chord length of the nested configuration. The slat and flap are deflected 25 and 20 deg, respectively, as shown in Fig. 2. Flow conditions are $M_\infty = 0.197$, $\alpha = 20.18$ deg, $Re = 3.52 \times 10^6$. Transition locations are given in Table 1.

Tables 2 and 3 describe the grids used for the single-element airfoils (cases 1–3). The distance to the far-field boundary is 12 chords. We do not discuss the error this introduces, which is independent of the grid density and the spatial discretization. Grid A was generated using an elliptic grid generator. Grid B was generated by removing every second node in both coordinate directions from grid A, and grid C was similarly generated from grid B. This technique produces a sequence of grids suitable for a grid convergence study. The grids for the transonic cases (cases 2 and 3) have more nodes on the upper surface than the lower surface (but no clustering at the shock).

Table 1   Transition locations given as percentage of elemental chord

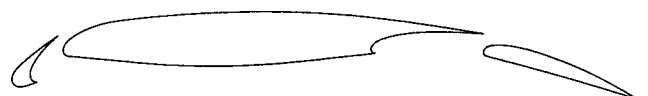| Element	Upper surface	Lower surface
Slat	5.00	——
Main	0.97	11.0
Flap	2.70	99.3

Fig. 2   High-lift test case A2.

Table 2   Grids for single-element subsonic case

Grid	Dimensions	Points on airfoil	Off-wall spacing ($\times 10^{-6}$)	Leading-edge clustering ($\times 10^{-3}$)	Trailing-edge clustering ($\times 10^{-3}$)
A	1057×193	801	0.23	0.1	0.5
B	529×97	401	0.53	0.2	1.0
C	265×49	201	1.2	0.4	2.0

Table 3   Grids for transonic cases

Grid	Dimensions	Points on airfoil (upper/lower)	Off-wall spacing ($\times 10^{-6}$)	Leading-edge clustering ($\times 10^{-3}$)	Trailing-edge clustering ($\times 10^{-3}$)
A	1025×225	501/301	0.23	0.1	0.25
B	513×113	251/151	0.53	0.2	0.5
C	257×57	126/76	1.2	0.4	1.0

Case 1   Case 3

Fig. 3   Grid C.

Fig. 4   Block decomposition for three-element test case.

Table 4   Multiblock grid densities

Grid	Number of nodes
A	255,295
B	183,721
C	126,125
D	72,837
E	51,749

Results and Discussion

In this section we compare results computed using the higher-order algorithm described with those computed using a second-order discretization for inviscid and viscous fluxes together with matrix dissipation, as well as second-order approximations for grid metrics and a second-order integration technique. Zingg at al.[25] showed that this second-order discretization produces numerical accuracy that is very similar to that obtained using either a third-order upwind-biased flux-difference-split scheme (with second-order metric terms) or the convective upstream split pressure scheme with second-order approximations for the viscous fluxes. Hence this second-order discretization is representative of the most popular current algorithms and provides a suitable benchmark for assessing the higher-order discretization.

It is important to recognize that the higher-order algorithm will generally not produce convergence consistent with higher-order accuracy in the presence of grid and flow singularities, such as those at the trailing edge of an airfoil. Although one might assume that the singularity leads to a lower-order error term that dominates the overall error and thus eliminates the advantage of the higher-order scheme, this is incorrect. The higher-order scheme can produce a second-order error, but with a much smaller coefficient than a second-order scheme. Problem 16.27 in Hirsch[42] provides an interesting example. The problem defines a converging-diverging nozzle that has a cross-sectional area with a discontinuous second derivative. Because the quasi-one-dimensional Euler equations have an exact solution for such flows, the error in a given numerical approximation can be precisely determined. We have solved for a subsonic flow through this nozzle using both second-order centered differences with third-order matrix dissipation and fourth-order centered differences with third-order matrix dissipation. For smoothly varying cross-sectional area distributions the former scheme produces a second-order convergence rate as the grid is refined, whereas the latter scheme produces third-order convergence, as expected. When these schemes are applied to the nozzle with a discontinuous second derivative, both produce second-order convergence, but the higher-order scheme produces much smaller errors on a given grid. Consequently, in this paper we will concentrate on local and global solution errors on various grids, rather than demonstrating that a specific order of accuracy is actually achieved. Of particular relevance is the comparison of errors on the coarsest grids (grid C for the single-element cases, grids D and E for the multielement case), which are typical of those used in practice.
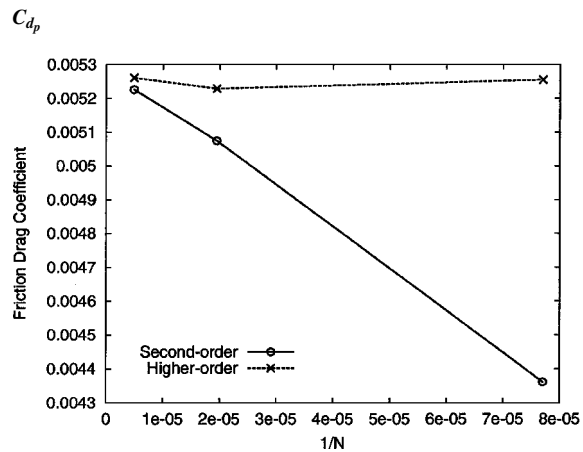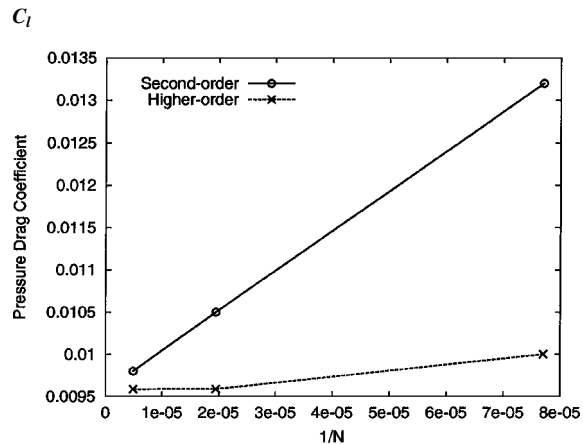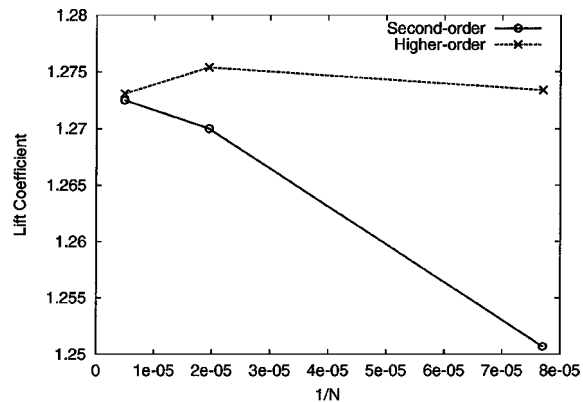
Figure 3 shows grid C around the NACA 0012 airfoil used for case 1 and grid C around the RAE 2822 airfoil used for case 3. Grid C has a node density suitable for practical computations, with less than 15,000 nodes. For all cases the y^+ value at the first point from the surface is less than one, where y^+ is the standard law-of-the-wall coordinate, and therefore there are a few grid points in the laminar sublayer of the turbulent boundary layers.

For the multielement configuration five grids were generated independently. Each grid consists of 27 blocks, as shown in Fig. 4, and the outer boundary is 24 chords from the airfoil surface. The grid densities, ranging from 255,295 nodes in the finest grid to 51,749 nodes in the coarsest grid, are given in Table 4. For all grids the streamwise grid spacing is $5 \times 10^{-4}c$ at the trailing edge of each element. Similarly the off-wall spacing in the normal direction is 10^{-6} chords for all five grids. These grids do not provide a family in the same sense as grids A, B, and C in the single-element cases. Use of such a family is impractical because of the high grid densities involved. Nevertheless, these five grids give a good indication of the levels of accuracy that can be achieved using grids of varying density.

C_l

C_{d_p}
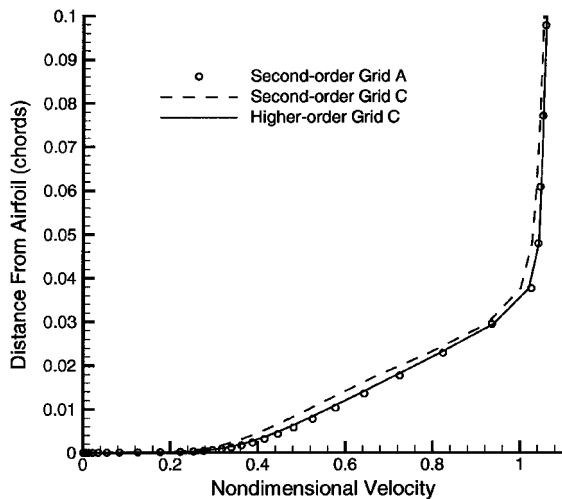
C_{d_f}

Fig. 5   Grid convergence for case 1.

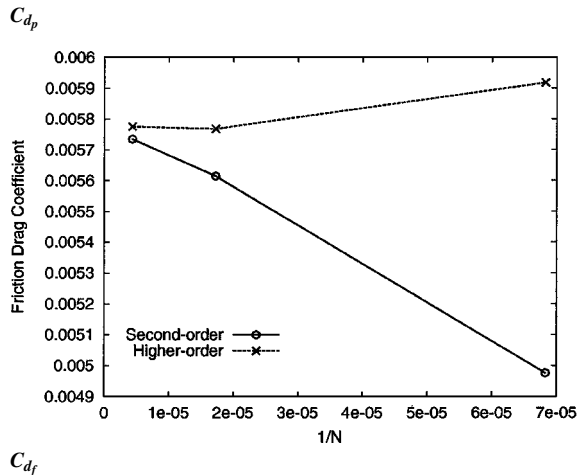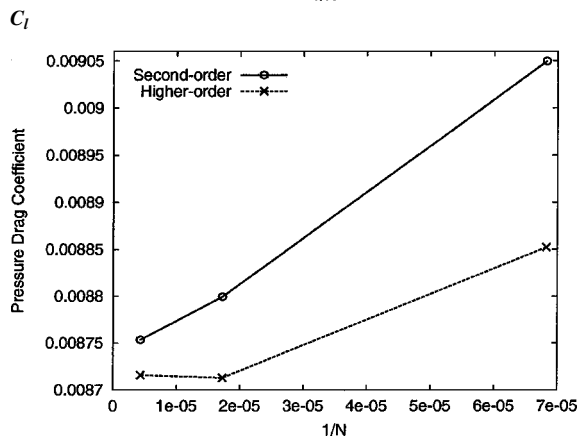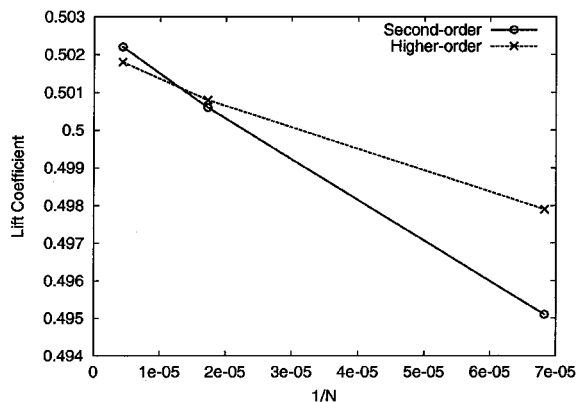**Fig. 6   Boundary-layer velocity profiles on the upper surface at 85% chord: case 1.**

C_l

C_{d_p}

C_{d_f}

Fig. 7   Grid convergence for case 2.

Figure 5 shows the lift, pressure drag, and skin-friction computed for case 1 using the higher-order and second-order algorithms on grids A, B, and C. They are plotted vs $1/N$, where N is the number of grid nodes. Agreement between the two algorithms on grid A is good, indicating that numerical errors are very small on this grid. Thus grid A provides a reference for estimating numerical errors on grids B and C. The error in lift from the second-order computation on grid C is roughly 1.7%, whereas that from the higher-order computation is much smaller. The errors in the drag components are much larger. The pressure-drag error from the higher-order scheme is less than 5% on grid C and well below 1% on grid B, whereas that from the second-order scheme is over 30% on grid C and near 7% on grid B. The friction drag error from the higher-order scheme is under 1% on both grids B and C, whereas that from the second-order scheme exceeds 15% on grid C and is roughly 3% on grid B. For this case the higher-order algorithm produces smaller errors on grid C than the second-order algorithm on grid B, which has four times as many nodes. Figure 6 displays computed boundary-layer velocity profiles on the upper surface near the trailing edge. The symbols show the second-order solution on grid A, which is indistinguishable from

C_l

C_{d_p}

C_{d_f}

Fig. 8   Grid convergence for case 3.

Fig. 9   Pressure coefficient on the upper surface; RAE 2822 airfoil, $M_\infty = 0.754$, $\alpha = 2.57$ deg.

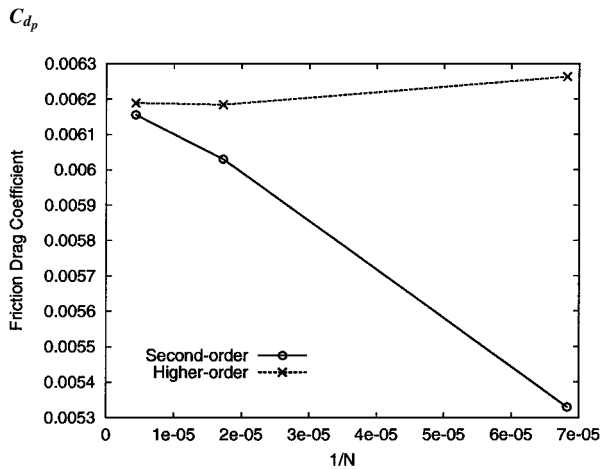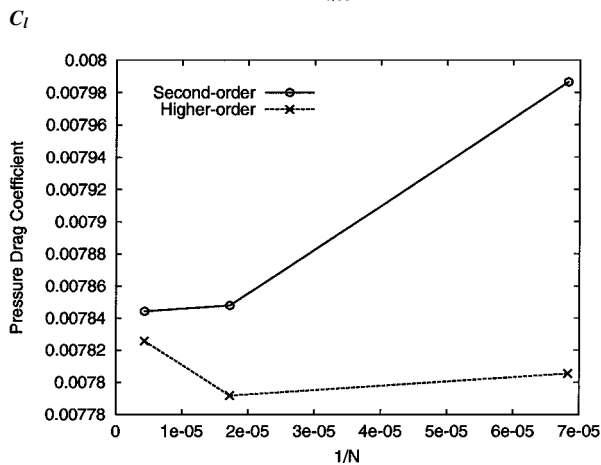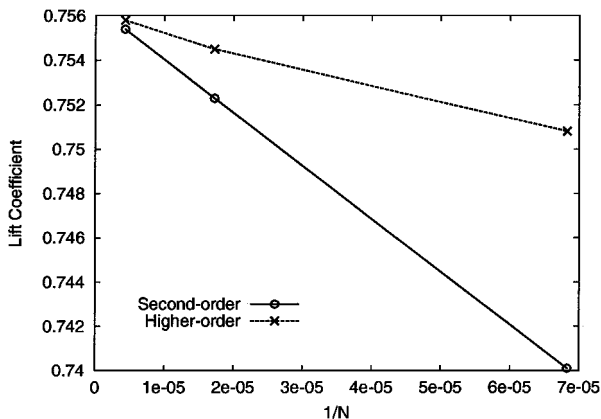Fig. 10   Boundary-layer velocity profiles on the upper surface at 95% chord; RAE 2822 airfoil, $M_\infty = 0.754$, $\alpha = 2.57$ deg.

the higher-order solution on grid A, with every fourth point plotted. The second-order results computed on grid C are seen to deviate significantly from this reference, whereas the higher-order solution is nearly grid independent.

Grid convergence studies for the two transonic cases (cases 2 and 3) are shown in Figs. 7 and 8. On grid C the higher-order algorithm produces errors in lift below 1% for both cases, whereas the second-order algorithm produces errors of roughly 1 and 2% for cases 2 and 3, respectively. For the drag components the second-order algorithm produces significant errors on grid C, especially in friction drag. The drag components computed using the higher-order algorithm on grid C are much smaller and are comparable to those computed using the second-order algorithm on grid B.

The higher-order results for the transonic cases indicate that the first-order numerical dissipation used to prevent oscillations near shock waves does not produce significant errors. To examine this further, we consider an additional transonic test case with a somewhat stronger shock wave. The flow parameters are as follows: RAE
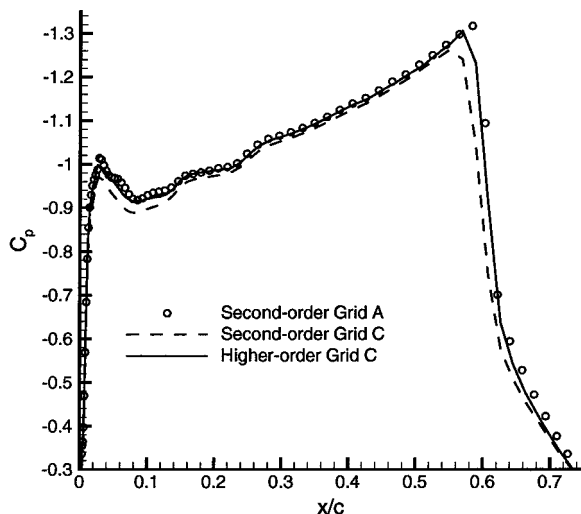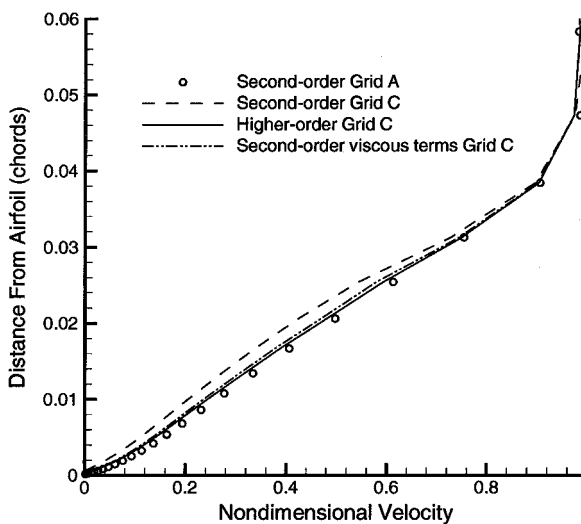
2822 airfoil, $M_\infty = 0.754$, $\alpha = 2.57$ deg, $Re = 6.2 \times 10^6$, laminar-turbulent transition at 0.03 chords on both surfaces.

Figure 9 shows the pressure distribution over a portion of the upper surface. On grid A the second-order and higher-order results are indistinguishable; only the second-order results are shown. The second-order solution on grid C shows significant errors, both at the shock and near the leading edge. The higher-order solution on grid C lies much closer to the grid A solution. Similar results are seen in Fig. 10, which shows computed boundary-layer profiles on the upper surface near the trailing edge. The second-order grid C solution deviates substantially from the grid A solution, whereas the higher-order solution computed on grid C, although not completely grid independent, is much more accurate. Figure 10 also shows the boundary-layer profile computed using the higher-order algorithm with a second-order approximation for the viscous terms (labeled "second-order viscous terms"). Although raising the inviscid fluxes and grid metrics to higher order produces the majority of the error reduction, this figure shows that the higher-order approximations to the viscous fluxes also reduce the error noticeably.

The error reduction obtained using the higher-order discretization for these flows over single-element airfoils with the Spalart–Allmaras turbulence model is similar to that reported by Zingg et al.[25] using the algebraic Baldwin–Lomax model. This demonstrates that the first-order treatment of the convective terms in the Spalart–Allmaras model does not undermine the accuracy of the higher-order discretization.
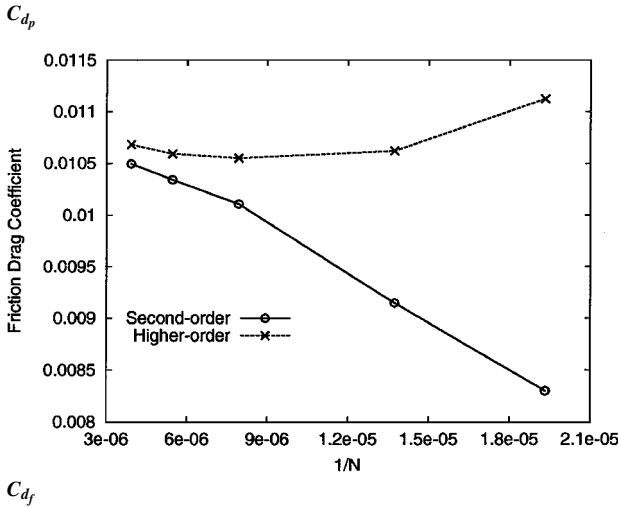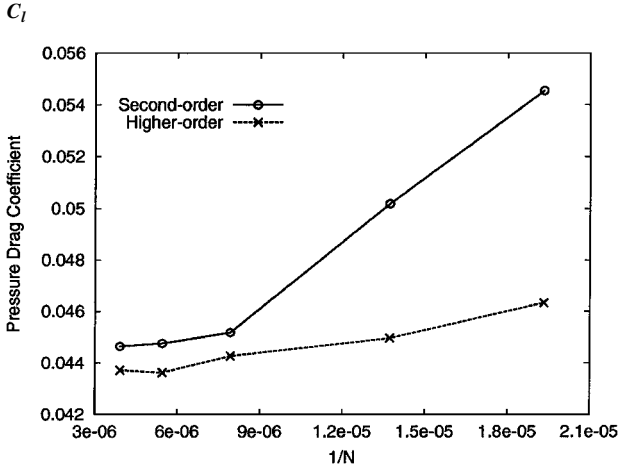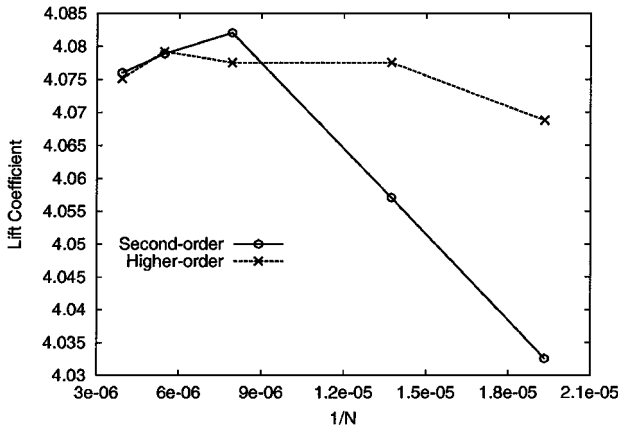
Fig. 11   Grid convergence for case 4.

C_l

C_{d_p}

C_{d_f}

Fig. 12   Pressure distribution for the three-element geometry.
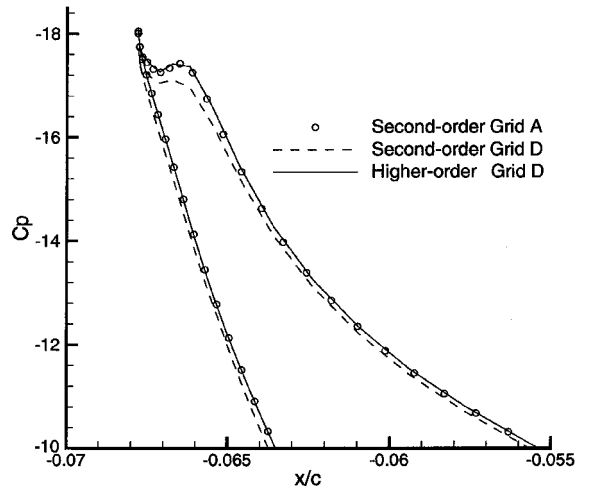
Fig. 13   Pressure distribution on upper surface of slat.

Figure 11 shows the dependence of the lift and drag components on the number of grid nodes for the three-element high-lift configuration. Compared to the solution on grid A, the errors in lift coefficient are modest for both discretization algorithms, with the higher-order scheme being significantly more accurate than the second-order scheme on grids D and E. On grid D the errors in both drag components for the higher-order scheme are below 3%, whereas the errors in the second-order results exceed 12%. On grid E, the coarsest grid studied, the errors in the drag components for the higher-order scheme are below 6%, whereas the errors in the second-order computation exceed 20%. For all quantities the higher-order results computed on grid D are comparable to the second-order results on grid A, which has over three times as many nodes.

Figure 12 shows the experimental and computed surface pressure distributions for the three-element airfoil configuration. The result computed using the second-order scheme on grid A, which is indistinguish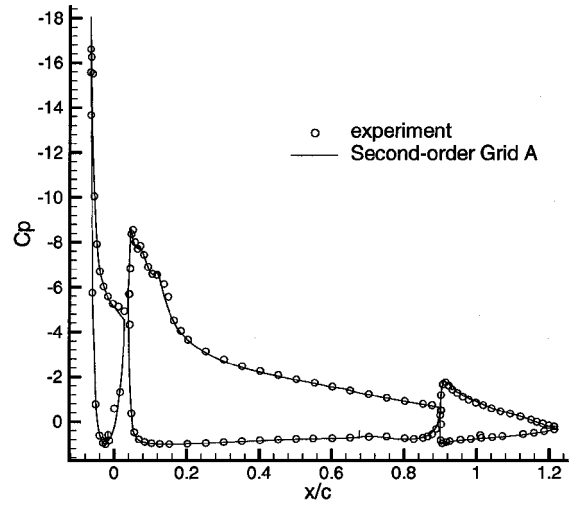able from the higher-order result on the same grid, shows excellent agreement with the experimental data. A portion of the upper surface pressure distribution of the slat is shown in Fig. 13. On grid D the second-order scheme does poorly at computing the minimum pressure. The higher-order computation on grid D is very close to the second-order computation on grid A. Similar results are found on the main element as well.

Figure 14 shows boundary-layer velocity profiles at the trailing edge of the flap. For the second-order solution on grid A, every third grid point is plotted. The profile can be divided into four regions: 1) the first 2.5% of chord above the flap surface corresponds to the flap boundary layer; 2) the region between 2.5 and 10% of chord corresponds to the wake from the main element; 3) the region between 10 and 18% of chord corresponds to the wake from the slat; and 4) beyond 18% of chord above the flap surface, the flow slowly returns to freestream conditions. Given the superior results obtained using the higher-order scheme for the single-element cases, the higher-order result on grid A is taken as the reference solution. Region 1 appears to be adequately resolved for both discretization schemes, even on grid D. In region 2 the higher-order result on grid D is more accurate than the second-order result on grid A. In region 3 the error in the second-order result on grid D is quite large and increases in region 4. The second-order result on grid A and the higher-order result on grid D provide comparable accuracy in regions 3 and 4. The second-order grid A result is slightly better in region 3, whereas the higher-order grid D result is slightly better in region 4. Nonetheless, the higher-order scheme is in excellent agreement with the reference solution using a grid with only 73,000 nodes.

The results presented demonstrate that the higher-order algorithm produces much smaller numerical errors than the second-order

algorithm on a given grid. For the single-element cases the higher-order solutions on grid C are comparable to the second-order solutions computed on grid B, which has four times as many nodes. For the multielement case the higher-order solution on grid D is comparable to the second-order solution on grid A, which has over three times as many nodes. To examine the improvement in efficiency, we must consider the cost of the two algorithms. In terms of memory, there is very little overhead associated with the higher-order algorithm. Therefore, the reduced grid density requirements of the higher-order algorithm translate directly into savings in memory. With respect to computing time, the higher-order algorithm requires 6 to 7% more time per iteration. Convergence histories (on grid C for cases 1–3, grid D for case 4) are displayed in Fig. 15. Typically,

the two algorithms converge similarly for the first three to five orders of magnitude reduction in residual, and the higher-order algorithm converges somewhat more slowly after that. Convergence of lift and drag is typically achieved after four to five orders of residual reduction. Therefore, the extra cost associated with the higher-order algorithm is quite small, and the higher-order algorithm produces solutions of a given accuracy much more efficiently than the second-order algorithm.

Conclusions

We have presented a stable, accurate, and robust higher-order spatial discretization for aerodynamic flows and compared its efficiency with that of a well-established second-order discretization. A key aspect of the higher-order algorithm is that almost all approximations are raised to a level of accuracy consistent with third-order global accuracy. The primary conclusion is that the higher-order algorithm is much more efficient than the second-order algorithm, requiring substantially fewer grid nodes to reduce numerical errors to specified levels for both subsonic and transonic flows. Typically, the higher-order discretization reduces the computing expense by a factor of three to four.

The success of the higher-order discretization suggests several avenues for future work:

1) Extension to three dimensions, where even larger benefits can be expected, can be considered.

2) Even higher-order discretizations, including compact schemes, can be considered. For example, the seven-point scheme of Zingg et al.,[7] which includes a sixth-order antisymmetric term and a fifth-order dissipative term, could be applied to steady aerodynamic flows. However, it is important to identify the largest sources of error in the current higher-order discretization before proceeding towards even higher-order schemes. For transonic flows if the first-order numerical dissipation at shocks is now the largest source of error, then there will be little benefit from increasing the order further. Furthermore, higher-order numerical boundary schemes could
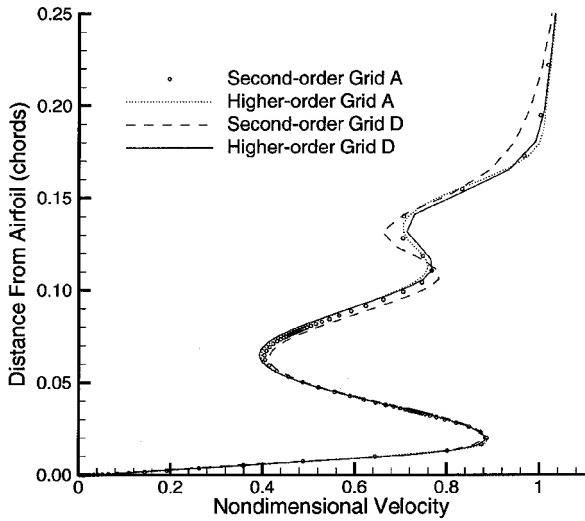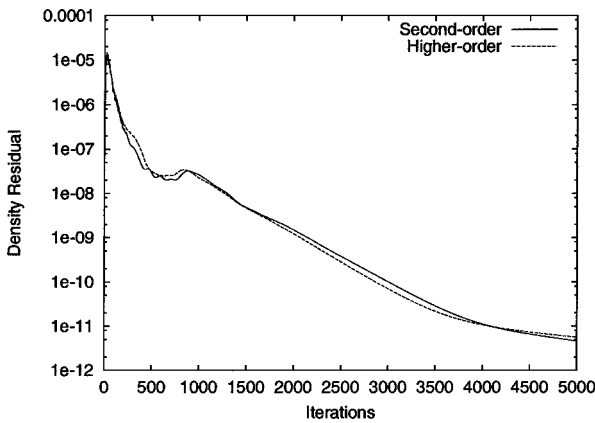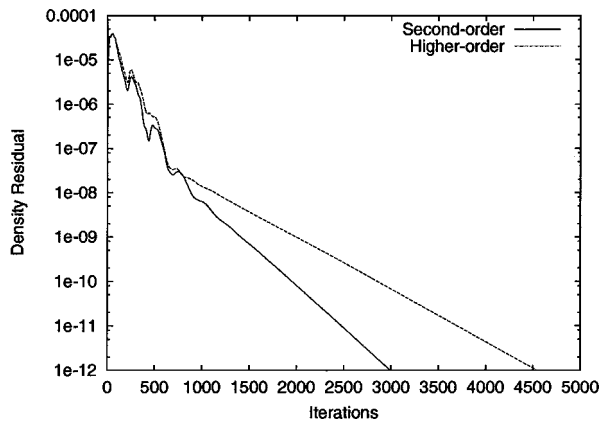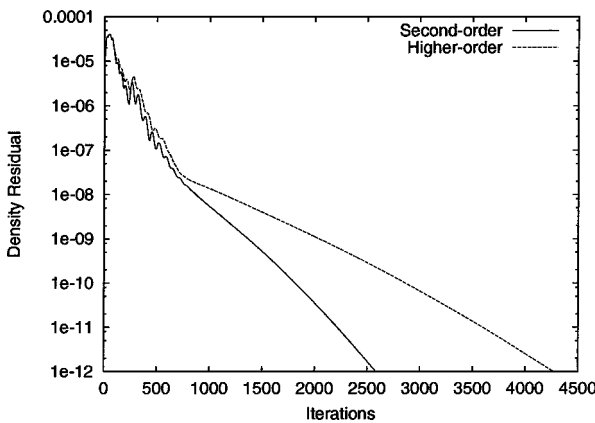

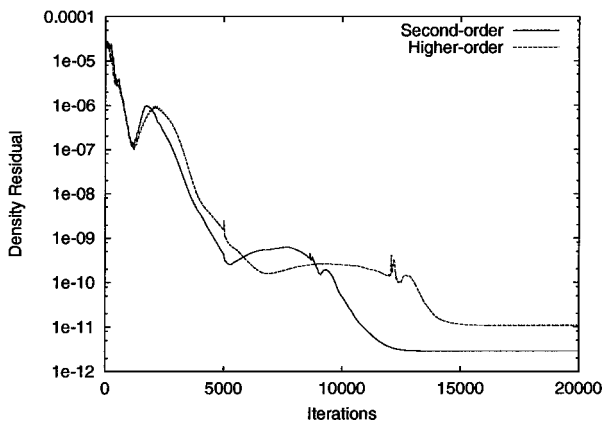**Fig. 14   Boundary-layer profile: upper surface of flap at trailing edge.**

Case 1

Case 3

Case 2

Case 4

Fig. 15   Residual histories on grid C.

slow convergence and reduce robustness. Similar comments apply to a higher-order numerical dissipation scheme. Finally, given that turbulence models typically require a grid point located near $y^+ = 1$, there is a physical limit to the amount the grids can be coarsened, independent of numerical error.

3) Methodologies for estimating local and global solution errors and local approximation errors need to be further developed. This information can be used in the generation and adaptation of grids. Furthermore, quantifying the contribution of various sources of error can help to guide further scheme development.

References

[1]Kreiss, H. -O., and Oliger, J., "Comparison of Accurate Methods for the Integration of Hyperbolic Equations," *Tellus*, Vol. 24, No. 3, 1972, pp. 199–215.

[2]Swartz, B., and Wendroff, B., "The Relative Efficiency of Finite Difference and Finite Element Methods," *SIAM Journal on Numerical Analysis*, Vol. 11, No. 5, 1974, pp. 979–993.

[3]Rai, M. M., and Moin, P., "Direct Numerical Simulation of Transition and Turbulence in a Spatially Evolving Boundary Layer," *Journal of Computational Physics*, Vol. 109, No. 2, 1993, pp. 169–192.

[4]Zhong, X., "High-Order Finite-Difference Schemes for Numerical Simulation of Hypersonic Boundary-Layer Transition," *Journal of Computational Physics*, Vol. 144, No. 2, 1998, pp. 662–709.

[5]Ekaterinaris, J. A., "Implicit, High-Resolution, Compact Schemes for Gas Dynamics and Aeroacoustics," *Journal of Computational Physics*, Vol. 156, No. 1, 2000, pp. 272–299.

[6]Wells, V. L., and Renaut, R. A., "Computing Aerodynamically Generated Noise," *Annual Review of Fluid Mechanics*, Vol. 29, 1997, pp. 161–199.

[7]Zingg, D. W., Lomax, H., and Jurgens, H. M., "High-Accuracy Finite-Difference Schemes for Linear Wave Propagation," *SIAM Journal on Scientific Computing*, Vol. 17, No. 2, 1996, pp. 328–346.

[8]Zingg, D. W., "Comparison of High-Order and Optimized Finite-Difference Methods for Simulating Linear Wave Phenomena," *SIAM Journal on Scientific Computing*, Vol. 22, No. 2, 2000, pp. 476–502.

[9]Rangwalla, A. A., and Rai, M. M., "A Multi-Zone High-Order Finite-Difference Method for the Navier–Stokes Equations," AIAA Paper 95-1706, June 1995.

[10]Visbal, M. R., and Gaitonde, D. V., "High-Order-Accurate Methods for Complex Unsteady Subsonic Flows," *AIAA Journal*, Vol. 37, No. 10, 1999, pp. 1231–1239.

[11]Rigby, D. L., "Compact Spatial Differencing and Subiteration Time Marching in the PARC Code," AIAA Paper 96-0385, Jan. 1996.

[12]Treidler, E. B., and Childs, R. E., "High-Accuracy Spatial Discretization Schemes for CFD," AIAA Paper 97-0541, Jan. 1997.

[13]Treidler, E. B., Ekaterinis, J., and Childs, R. E., "Efficient Solution Algorithms for High-Accuracy Central Difference CFD Schemes," AIAA Paper 99-0302, Jan. 1999.

[14]Rai, M. M., and Chakravarty, S. R., "Conservative High-Order-Accurate Finite-Difference Methods for Curvilinear Grids," AIAA Paper 93-3380, June 1993.

[15]Rai, M. M., "Navier–Stokes Simulations of Rotor-Stator Interaction Using Patched and Overlaid Grids," *Journal of Propulsion and Power*, Vol. 3, No. 5, 1987, pp. 387–396.

[16]De Rango, S., and Zingg, D. W., "Aerodynamic Computations Using a Higher-Order Algorithm," AIAA Paper 99-0167, Jan. 1999.

[17]De Rango, S., and Zingg, D. W., "Further Investigation of a Higher-Order Algorithm for Aerodynamic Computations," AIAA Paper 2000-0823, Jan. 2000.

[18]Jameson, A., Schmidt, W., and Turkel, E., "Numerical Solutions of the Euler Equations by Finite Volume Methods Using Runge–Kutta Time Stepping," AIAA Paper 81-1259, June 1981.

[19]Allmaras, S. R., "Contamination of Laminar Boundary Layers by Artificial Dissipation in Navier–Stokes Solutions," *Numerical Methods for Fluid Dynamics*, edited by M. J. Baines and K. W. Morton, Clarendon, Oxford, 1993.

[20]Frew, K., Zingg, D. W., and De Rango, S., "Artificial Dissipation Schemes for Viscous Airfoil Computations," *AIAA Journal*, Vol. 36, No. 9, 1998, pp. 1732–1734.

[21]Roe, P. L., "Approximate Riemann Solvers, Parameter Vectors, and Difference Schemes," *Journal of Computational Physics*, Vol. 43, 1981, pp. 357–372.

[22]Swanson, R. C., and Turkel, E., "On Central-Difference and Upwind Schemes," *Journal of Computational Physics*, Vol. 101, 1992, pp. 292–306.

[23]Roache, P. J., *Verification and Validation in Computational Science and Engineering*, Hermosa, Albuquerque, NM, 1998.

[24]Zingg, D. W., "Grid Studies for Thin-Layer Navier–Stokes Computations of Airfoil Flowfields," *AIAA Journal*, Vol. 30, No. 10, 1992, pp. 2561–2564.

[25]Zingg, D. W., De Rango, S., Nemec, M., and Pulliam, T. H., "Comparison of Several Discretizations for the Navier–Stokes Equations," *Journal of Computational Physics*, Vol. 160, No. 2, 2000, pp. 683–704.

[26]Jameson, A., "Analysis and Design of Numerical Schemes for Gas Dynamics I: Artificial Diffusion, Upwind Biasing, Limiters and Their Effect on Accuracy and Multigrid Convergence," *International Journal of Computational Fluid Dynamics*, Vol. 4, 1995, pp. 171–218.

[27]Jameson, A., "Analysis and Design of Numerical Schemes for Gas Dynamics II: Artificial Diffusion and Discrete Shock Structure," *International Journal of Computational Fluid Dynamics*, Vol. 5, 1995, pp. 1–38.

[28]Spalart, P. R., and Allmaras, S. R., "A One-Equation Turbulence Model for Aerodynamic Flows," AIAA Paper 92-0439, Jan. 1992.

[29]Nelson, T. E., Godin, P., De Rango, S., and Zingg, D. W., "Flow Computations for a Three-Element Airfoil System," *Canadian Aeronautics and Space Journal*, Vol. 45, No. 2, 1999, pp. 132–139.

[30]Pulliam, T. H., "Efficient Solution Methods for the Navier–Stokes Equations," Lecture Notes for the Von Karman Inst. for Fluid Dynamics Lecture Series, Brussels, Jan. 1986.

[31]Jespersen, D., Pulliam, T., and Buning, P., "Recent Enhancements to OVERFLOW," AIAA Paper 97-0644, Jan. 1997.

[32]Pulliam, T. H., and Chaussee, D. S., "A Diagonal Form of an Implicit Approximate-Factorization Algorithm," *Journal of Computational Physics*, Vol. 39, 1981, pp. 347–363.

[33]Beam, R., and Warming, R. F., "An Implicit Finite-Difference Algorithm for Hyperbolic Systems in Conservation Law Form," *Journal of Computational Physics*, Vol. 22, 1976, pp. 87–110.

[34]Nelson, T. E., Zingg, D. W., and Johnston, G. W., "Compressible Navier–Stokes Computations of Multi-Element Airfoil Flows Using Multiblock Grids," *AIAA Journal*, Vol. 32, No. 3, 1994, pp. 506–511.

[35]Godin, P., Zingg, D. W., and Nelson, T. E., "High-Lift Aerodynamic Computations with One- and Two-Equation Turbulence Models," *AIAA Journal*, Vol. 35, No. 2, 1997, pp. 237–243.

[36]Gustafsson, B., "The Convergence Rate for Difference Approximations to Mixed Initial Boundary Value Problems," *Mathematics of Computation*, Vol. 29, No. 130, 1975, pp. 396–406.

[37]Barth, T. J., "Aspects of Unstructured Grids and Finite-Volume Solvers for the Euler and Navier–Stokes Equations," Lecture Notes for the Von Karman Inst. for Fluid Dynamics Lecture Series, 1994-05, Brussels, 1994.

[38]Malcolm, M. A., and Simpson, R. B., "Local Versus Global Strategies for Adaptive Quadrature," *ACM Transactions on Mathematical Software*, Vol. 1, No. 2, 1975, p. 129.

[39]Gregory, N., and O'Reilly, C. L., "Low-Speed Aerodynamic Characteristics of NACA 0012 Airfoil Section, Including the Effects of Upper-Surface Roughness Simulating Hoar Frost," Aeronautical Research Council, Repts. and Memoranda 3726, London, Jan. 1970.

[40]Cook, P. H., MacDonald, M. A., and Firmin, M. C. P., "Aerofoil RAE 2822—Pressure Distributions, and Boundary-Layer and Wake Measurements," AR-138, AGARD, May 1979.

[41]Moir, I. R. M., "Measurements on a Two-Dimensional Aerofoil with High-Lift Devices," AR 303, AGARD, Aug. 1994.

[42]Hirsch, C., *Numerical Computation of Internal and External Flows, Volume 2: Computational Methods for Inviscid and Viscous Flows*, Wiley, New York, 1990, p. 221.

J. Kallinderis
Associate Editor